Photoemission Insight on Narrow Band Gap PbS Quantum Dots Relevant for Infrared Imaging

Huichen Zhang, Nicolas Ledos, Mariarosa Cavallo, Erwan Bossavit, Adrien Khalili, Leonardo Curti, Xiang Zhen Xu, Erwan Dandeu, James Utterback, Sandrine Ithurria, et al.

Photoemission Insight on Narrow Band Gap PbS Quantum Dots Relevant for Infrared Imaging

Huichen Zhang[1], Nicolas Ledos[1], Mariarosa Cavallo[1], Erwan Bossavit[2], Adrien Khalili[1], Leonardo Curti[3], Xiang Zhen Xu[3], Erwan Dandeu[1], James K. Utterback[1], Sandrine Ithurria[3], Christophe Delerue[4], Debora Pierucci[1], Pavel Dudin[2], José Avila[2], Mathieu G. Silly[2], Emmanuel Lhuillier[1*]

[1]Sorbonne Université, CNRS, Institut des NanoSciences de Paris, 4 place jussieu, 75005 Paris, France
[2] Synchrotron SOLEIL, L'Orme des Merisiers, Départementale 128, 91190 Saint-Aubin, France.
[3] Laboratoire de Physique et d'Etude des Matériaux, ESPCI, PSL Research University, Sorbonne Université, CNRS, 10 rue Vauquelin, 75005 Paris, France.
[4]Univ. Lille, CNRS, Centrale Lille, Univ. Polytechnique Hauts-de-France, Junia, IEMN, 59000 Lille, France.

Abstract: In recent years, the interest for narrow band gap colloidal quantum dots (CQDs) has shifted from materials optimized for solar cells (with $E_G \approx 1.2$ eV) to materials with properties at longer wavelengths. This shift necessitates a systematic investigation of their electronic properties to optimize photodiode design effectively. In this study, we utilized X-ray photoemission to systematically determine how the band gap (with absorption maximum wavelengths of 1000, 1200, 1400, and 1550 nm) and surface chemistry (short halides and thiols) influence the band alignment and the core levels in PbS nanocrystals. Our research provides evidence for a shift from quasi-intrinsic behavior for the narrowest band gap to an exclusively *n*-type nature for the particles with largest size, potentially indicating the emergence of degenerate doping. Core level analysis also revealed that the effect of ligands extends beyond dipole behavior, inducing charge transfer leading to the formation of metallic islands, which might be detrimental to photodetection. Furthermore, by employing scanning photoemission microscopy, we gained direct access to the photodiode's built-in potential—a parameter typically obtained through indirect modeling. We then discussed how particle size influences this property. This study lays the foundation for a more rational design of PbS CQD-based photodiodes operating in the short-wave infrared spectrum.

Keywords: quantum dots, infrared, electronic structure, photoemission.

*To whom correspondence should be sent: el@insp.upmc.fr

INTRODUCTION

Among colloidal quantum dots (CQDs), PbS-based[1] nanocrystals stand out as the material of choice. Their synthesis can be achieved with high accuracy, enabling size dispersity as low as 3%,[2] making it highly valuable for self-assembling[3] these particles into superlattices.[4–6] Additionally, its narrow band gap nature allows for addressing infrared wavelengths,[7,8] which has generated significant interest in the field of optoelectronics,[9] especially in solar cell design.[10] For this application, particles with a size[11,12] of around 3 nm are chosen, aligning the band edge energy (≈1.2 eV) with the Queisser-Shockley criteria for single junction solar cells.

To build a solar cell using an optically active layer of CQDs, a diode needs to be formed. Initially, this was achieved through Schottky contacts. However, improved photodiodes based on *pn* junctions were developed through systematic studies on the impact of capping ligands on band alignment, employing ultraviolet photoemission techniques. Brown *et al.*[13] provided experimental evidence showing that the surface dipole associated with capping ligands induces a relative displacement of the valence band concerning the Fermi level, allowing tunability of the carrier density. The energy shift is given by $\Delta E = \frac{N.\mu}{\varepsilon_0 \varepsilon_r}$ (1), where μ represents the dipole magnitude, N denotes the surface density of dipoles, ε_0 is the vacuum permittivity, and ε_r is the dielectric constant[14,15]. This systematic approach was immediately utilized to design optimized *pn* junctions, leading to record power conversion efficiencies.[16]

In a groundbreaking study, Chuang *et al.* proposed combining an iodine-capped PbS CQD layer with a thiol-capped layer, utilized as *n*-type and *p*-type layers respectively, to form the *pn* junction. This work has opened up possibilities for engineering dipoles to maximize the energy shift.[17] However, while extensive efforts have been dedicated to PbS CQDs with this specific band gap value of 1.2 eV, interest in infrared CQDs has expanded to longer wavelengths.

Indeed, due to their inorganic core, PbS CQDs are infrared active, in contrast to conductive organic polymers. Additionally, their cost-efficient growth and large-scale processability make them highly relevant for infrared imaging applications. [18–20] Traditional infrared imagers rely on CMOS read-out circuits coupled with infrared-active thin films, usually grown epitaxially. However, these fabrication methods suffer from high growth costs and constraints imposed by the substrate, such as limited spectral tunability, elevated costs, higher concentrations of heavy metals in comparison to thin films, and reduced optical transparency. These limitations necessitate alternative methods, particularly for applications where cost is a critical factor, such as single-use sensors and the automotive industry.

Consequently, there is a pressing need to expand the research conducted by Brown *et al*.[13] to encompass nanocrystals with smaller band gaps relevant for infrared imaging[21–25] and with ligands that are short enough to be compatible with photoconduction. In this study, we considered four CQD sizes with band-edges at 1000 nm, 1200 nm, 1400 nm (matching the water absorption line), and 1550 nm (matching telecom applications). For all sizes, we tested six capping ligands with short lengths to ensure compatibility with charge transport and photoconduction. Systematic measurements were conducted to assess their band alignment, which included determining the work function through the secondary electron cutoff and identifying the energy value of the valence band maximum. Additionally, core level measurements were performed to reveal effects missed by ultraviolet photoemission spectroscopy (UPS), such as charge transfer and chemical analysis.

Our analysis, in particular, unveiled a significant shift in properties from intrinsic behavior for the widest band gap to quasi-degenerately *n*-type doping for the largest size. Finally, we employed photoemission microscopy as a tool to directly measure the built-in potential from a PbS CQD-based *pn* junction. This enabled us to correlate the drop in the built-in potential with the emergence of degenerate *n*-type doping.

METHOD

Chemicals. Trioctylphosphine (TOP, Alfa Aesar, 90%), oleylamine (Alfa Aesar, 80-90%), lead chloride ($PbCl_2$, Alfa Aesar, 99%), sulfur powder (S, Alfa Aesar, 99.5%), oleic acid (OA, Alfa Aesar, 90%), 1,2 ethanedithiol (EDT, Fluka, 98.0%), ethanol absolute anhydrous (VWR), methanol (VWR, 99.8%), acetone (VWR), n-hexane (VWR), n-octane (SDS, 99%), toluene (VWR, 99.3%), N,N-dimethylformamide (DMF, VWR), ammonium iodine (NH_4I, Alfa Aesar, ≥ 99%), acetonitrile (VWR, ACS), butylamine (Alfa Aesar, 99%), isopropanol (IPA, VWR), 3-mercaptopropionic acid (MPA, Sigma-Aldrich, ≥99.9%), ammonium chloride (NH_4Cl, Alfa Aesar, 98%), Tetra-n-butylammonium iodide (TBAI, Merck KGaA, purity 98%), 1,4-Benzenedithiol (BDT, Alfa Aesar, 97%). All chemicals are used as received, except oleylamine which is centrifuged before use.

PbS 1000 synthesis: In a three-neck flask, 300 mg of $PbCl_2$, 100µL of TOP and 7.5 mL of OLA are mixed together and degassed, first at room temperature and then at 110 °C for 30 min. Meanwhile, 30 mg of sulfur powder are mixed with 7.5 mL of OLA until full dissolution and a clear orange solution is obtained. Then under N_2 at 68 °C, this solution of sulfur is quickly added to the flask. After 30 s, the reaction is quickly quenched by addition of 1 mL of oleic acid and 9 mL of hexane. The CQDs are precipitated with ethanol and redispersed in toluene. This washing step is repeated one more time. The solution is then centrifuged to remove the unstable phase. The supernatant is precipitated with methanol and redispersed in toluene.

PbS 1200 synthesis: In a three-neck flask, 300 mg of $PbCl_2$, 100 µL of TOP and 7.5 mL of OLA are mixed together and degassed, first at room temperature and then at 110 °C for 30 min. Meanwhile, 30 mg of sulfur powder are mixed with 7.5 mL of OLA until full dissolution and a clear orange solution is obtained. Then under N_2 at 100 °C, this solution of sulfur is quickly added to the flask. After 3 minutes, the reaction is quickly quenched by addition of 1 mL of oleic acid and 9 mL of hexane. The CQDs are precipitated with ethanol and redispersed in toluene. This washing step is repeated one more time. The solution is then centrifuged to remove the unstable phase. The supernatant is precipitated with methanol and redispersed in toluene.

PbS 1400 synthesis: In a three-neck flask, 300 mg of $PbCl_2$ and 7.5 mL of OLA are mixed together and degassed, first at room temperature and then at 110 °C for 30 min. Meanwhile, 30 mg of sulfur powder are mixed with 7.5 mL of OLA until full dissolution and a clear orange solution is obtained. Then under N_2 at 115 °C, this solution of sulfur is quickly added to the flask. After 4 minutes, the reaction is quickly quenched by addition of 1 mL of oleic acid and 9 mL of hexane. The CQDs are precipitated with ethanol and redispersed in toluene. This washing step is repeated one more time. The solution is then centrifuged to remove the unstable phase. The supernatant is precipitated with methanol and redispersed in toluene.

PbS 1550 Synthesis*:* In a three-neck flask, 300 mg of $PbCl_2$ and 7.5 mL of OLA are mixed together and degassed, first at room temperature and then at 110 °C for 30 min. Meanwhile, 30 mg of sulfur powder are mixed with 7.5 mL of OLA until full dissolution and a clear orange solution is obtained. Then under N_2 at 150 °C, this solution of sulfur is quickly added to the flask. After 15 minutes, the reaction is quickly quenched by addition of 1 mL of oleic acid and 9 mL of hexane. The CQDs are precipitated with ethanol and redispersed in hexane. Again, the CQDs are precipitated with ethanol and redispersed in hexane and a drop of OA. The cleaning is repeated a third time. Finally, the CQDs in hexane are then centrifuged to remove the unstable phase.

Thin film preparation: The gold-coated Si substrates (the gold layer is 80 nm thick) are cleaned in acetone via sonication and rinsed with acetone and IPA sequentially before N_2 flow drying. The substrates are then exposed to ozone plasma for 10 min to increase the surface wettability. The first layer of PbS film (≈30 nm) is deposited by spin coating. Then, the ligand exchange is achieved by dipping the PbS film in the target ligand exchange solution for 30 s and in pure ACN for 10 s, after which the films are spin-dried. The PbS deposition and ligand exchange are repeated one more time to fill the cracks and generate a continuous film (≈60 nm thick). The ligand exchange solutions are prepared as following: EDT (0.1% in ACN), MPA (0.1% in ACN), BDT (0.1% in ACN), NH_4Cl (1% in ACN), NH_4I (1% in ACN), TBAI (1% in ACN). For absorbance measurements, the films are prepared on glass substrates as well. To avoid oxidation, the films are deposited in a N_2-filled glovebox.

Infrared Absorption spectroscopy: For infrared spectroscopy, we use a ThermoFisher Nicolet iS50 in ATR (attenuated total reflection) mode. The spectra are averaged over 64 acquisitions and have a 4 cm^{-1} resolution. The light source is a halogen lamp, the beam splitter is CaF_2 and the detector an DTGS sensor.

TEM: A drop of diluted CQDs solution was drop-casted onto a copper grid covered with an amorphous carbon film. The grid was degassed overnight under secondary vacuum. Imaging was conducted using a JEOL 2010 transmission electron microscope operated at 200 kV.

X-ray photoemission measurements: Photoemission spectroscopy measurements are carried out at Tempo beamline of Synchrotron Soleil (France). Films of nanocrystals are spin-casted onto a gold coated Si substrate (the gold layer was 80 nm thick). The ligands of the nanocrystals are exchanged using the same procedure as for device fabrication to avoid any charging effects during measurements. Samples are introduced in the preparation chamber and degassed until a vacuum below 10^{-9} mbar is reached. Then samples are introduced in the analysis chamber. The signal is acquired by a MBS A-1 photoelectron analyzer equipped with a delay line detector developed by Elettra.[26] The acquisition is done at a constant pass energy (50 eV) within the detector. The photon energy of 150 eV is used for the acquisition of valence bands and work functions while 700 eV is used for the analysis of the core levels. A gold substrate is used to calibrate the Fermi energy. The absolute value of the incoming photon energy is determined by measuring the first and second orders of Au4f core level peaks. Then for a given analyzer pass energy, we measure the Fermi edge and set its binding energy as zero. The same shift is applied to all spectra acquired with the same pass energy. To determine the work function via the measurement of the secondary electrons (SE) edge, we apply an 18 V bias (this ensures that the SE have a kinetic energy higher than the analyzer vacuum level), whose exact value has been determined by looking at the shift of a Fermi edge.

The acquired core level data were processed by subtracting a Shirley/linear background and pseudo-Voight function (20% weighted Lorentzian contribution) for peak fitting. The values of the work functions were obtained via the determination of the energy value of the SE cutoff by extrapolation the edge of the peak respect to the zero baseline. The binding energy value of the valence band maxima with respect to the Fermi level was determined by finding the intersection of the linear extrapolation of the leading edge of the valence band spectra with the baseline.

X-ray Photoemission microscopy: is conducted on ANTARES beamline of Synchrotron SOLEIL. The synchrotron beam, which is ≈80 µm wide, is focused using a zone plate (*i.e.,* Fresnel lens). The latter is made to operate at low energy (around 100 eV), to obtain optimal focusing. In this case, the beam width at the sample position can be down to around 700 nm. The sample is then scanned and

the photoelectrons are collected using MBS A-1 hemispherical electron analyzer.[27] We used linearly horizontal polarized photons with a photon energy of 95 eV and all measurements were conducted at 200 K, with an energy resolution better than 30 meV. For all maps, angular dispersion of the analyzer (±15°) is neglected by integrating the spectra over all angles

RESULTS AND DISCUSSION

We initiated the study by growing a series of PbS colloidal quantum dots (CQDs) using the method developed by Moreels *et al*.[11] The reaction conditions, primarily the temperature and reaction time, were meticulously adjusted to tailor the particle excitonic peak, ranging from 1000 nm (matching materials relevant to solar cells) to longer wavelength: 1200, 1400, and 1550 nm, as illustrated in **Figure 1**a, S1 and table S1. This corresponds roughly to an increase in size from 3 nm for the bluest particles to 8 nm for the largest particles, as observed in the transmission electron microscopy (TEM) images depicted in **Figure 1**b-d.

Subsequently, the material was spin-coated onto a gold-coated silicon substrate, serving the purpose of preventing electrostatic charging in the sample during subsequent photoemission experiments. The PbS CQDs were then subjected to ligand exchange[28] using halides (NH_4Cl:ammonium chloride, NH_4I:ammonium iodine), TBAI:tributylammonium iodine), or thiols (MPA: mercapto propionic acid, EDT: ethanedithiol, and BDT: benzenedithiol). These ligands were selected for their short length, facilitating interparticle coupling and promoting the associated carrier mobility. For PbS CQDs with a band edge at 1000 nm, the combination of iodine and thiol represents a well-established strategy[16] to form n- and p-type layers, respectively

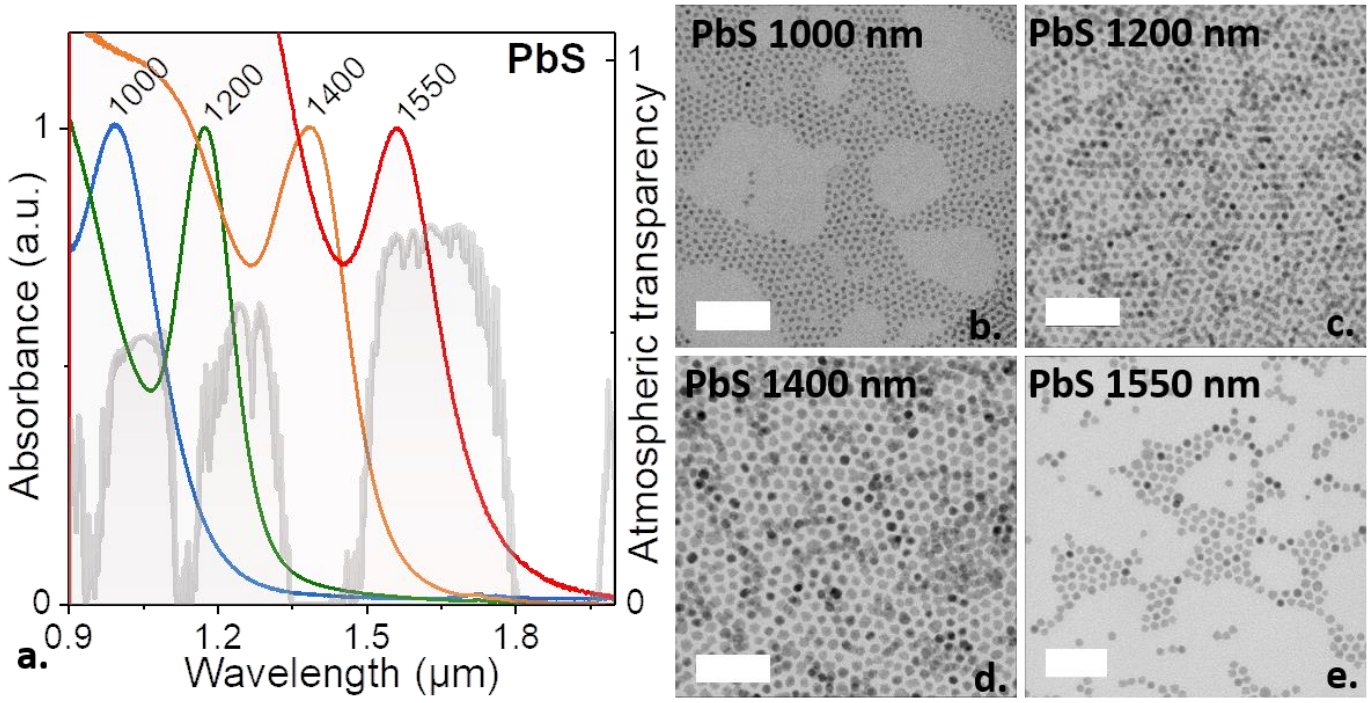

Figure 1 Short-wave infrared PbS CQDs. *a. Infrared absorption spectra for the four different sizes of CQD investigated and transparency of the atmosphere (grey line) over 10 km.[29] b-e are respectively TEM images for PbS CQDs with band-edge at 1000, 1200, 1400 and 1550 nm. Scale bars are 50 nm wide.*

We conducted a systematic investigation of core levels, valence bands, and cut-offs of secondary electrons for all samples using photoemission spectroscopy. A representative dataset for PbS CQDs with a 1400 nm band gap and TBAI ligands is provided in **Figure 2**, while data for all samples are

presented in Figures S2-S25. The survey spectrum (**Figure 2**a) confirms the presence of lead sulfide, along with carbon (from the alkyl chains of ligands), iodine, chlorine, and oxygen. The presence of oxygen results from the PbS material's strong tendency to oxidize, despite the preparation of thin films in a glove box and quick transfer to the ultra-high vacuum chamber to minimize exposure to air. Chlorine residues are due to the remnants of the lead precursor ($PbCl_2$, see Table S3), with higher amounts found in the smallest particles grown at lower temperatures, where the reaction yield is reduced. This explains why the smallest particles are alternatively grown using lead oleate as a precursor.[1,30] In contrast, the largest particles exhibit minimal traces of chloride, despite its use as a precursor.

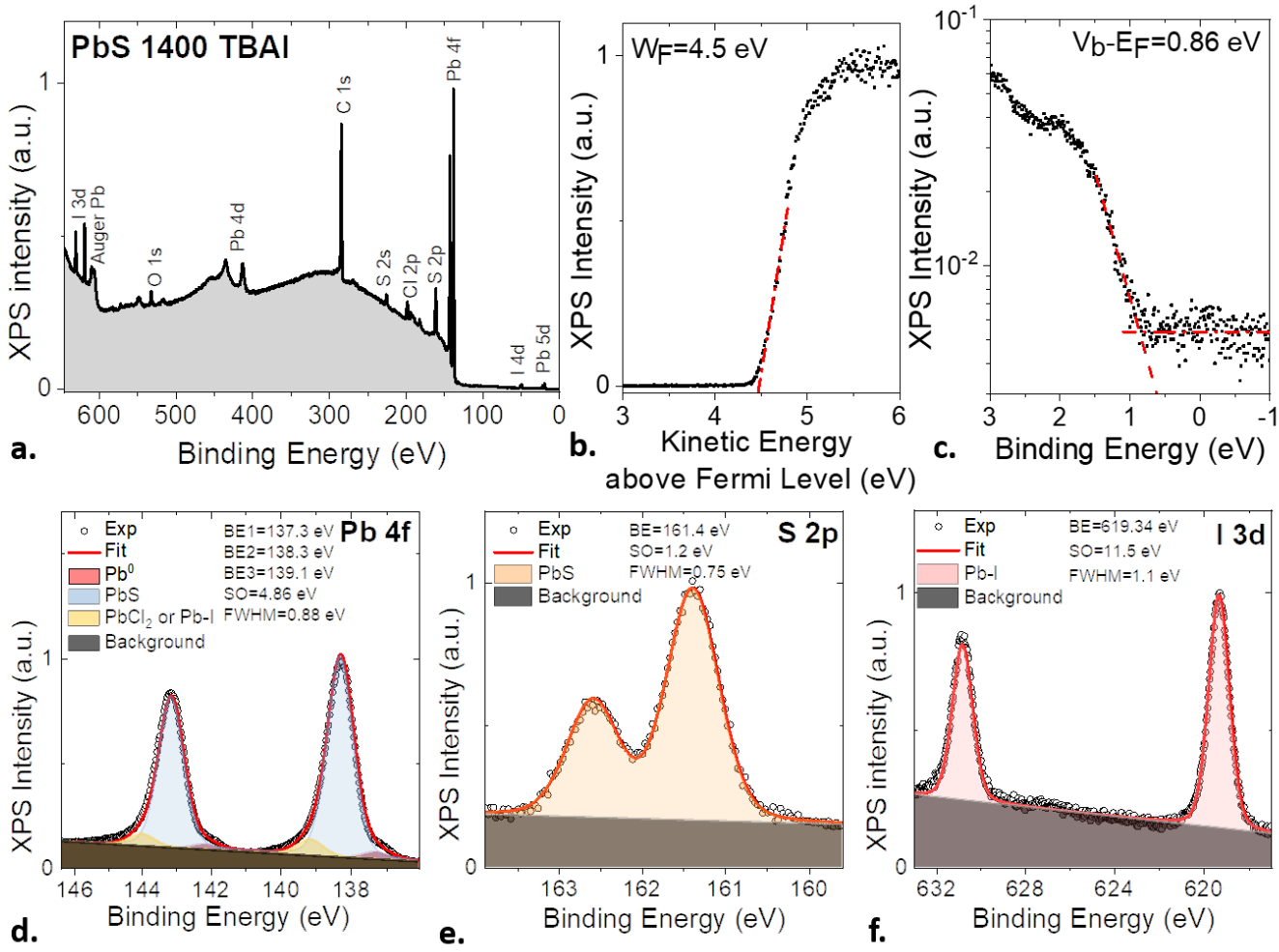

Figure 2 X-ray photoemission spectroscopy of PbS CQDs with 1400 nm band-edge and capped with TBAI*. a. Survey X-ray photoemission spectrum acquired using a 700 eV photon energy. b. Spectrum relative to the secondary electron cut-off. c. Spectrum relative to the valence band. d. Spectrum relative to Pb 4f state. e. Spectrum relative to the S 2p state. f. Spectrum relative to I 3d state.*

The state associated with lead will be extensively discussed in ***Figure 2****d and* **Figure 4**. The I 3d state (***Figure 2****f)* exhibits a single contribution with a 619.3 eV binding energy, a value typical for -1 redox state.[31] This suggests a single environment for the iodine on the PbS surface. The S 2p state (***Figure 2****e)* mostly displays a single contribution with a 161.4 eV binding energy, which matches the expected value for sulfur bound to lead.[31] There is nevertheless one clear exception, observed in samples capped with BDT (Figure S6, S18 and S24), where an additional feature at a higher binding energy of 163.6 eV is clearly present. This value is too small to result from the full oxidation of sulfide into sulfate, for which the expected binding energy is above 165 eV. This intermediate binding

energy highlights the weaker electron-donating ability of BDT compared to other thiols ligand, which comes from the negative charge on the sulfur being partially delocalized on the π-conjugated system. Following the approach outlined by Brown et al.,[13] we determined the effective band alignment for all sizes and compositions, as illustrated in ***Figure 2****b-c and* **Figure 3**a-d. Fermi level being a chemical potential, it becomes homogeneous over a diode stack, thus the Fermi energy is used as the reference zero binding energy point for energy levels. The valence band maximum (VBM) was determined from the low binding energy part of the photoemission spectrum, acquired at a lower photon energy (hv=150 eV) than the core level (hv=700 eV) to achieve a more surface-sensitive condition. We found that better determination of the valence band energy is obtained while fitting the density of state graph in logarithmic scale. The conduction band minimum (CBM) is determined relative to the valence band maximum by adding the optical band gap (determined after ligand exchange). This assumption is justified, considering the negligible excitonic corrections to the band gap in the case of PbS, attributed to its large dielectric constant.[14] Finally, the vacuum level was established based on the value of the work function.

For the smallest CQDs with a band edge at 1000 nm (**Figure 3**a), we observe a trend where halides tend to shift the Fermi level toward the upper part of the band gap (indicating n-type semiconductor behavior), whereas thiol ligands generate an opposite shift, moving the Fermi level toward the valence band. As the band gap decreases, the predominant trend becomes the observation of an n-type character for PbS,[23] regardless of the capping ligands, as shown in **Figure 3**c-e. The magnitude of the shift also tends to get reduced, a behavior that may be related to the change of facet with the particle size switching from (111) only for the smallest CQD to combination of (111) and (100) for the largest ones.[32]

The shift toward *n*-type agrees with field effect transistor measurements (Figure S26) that present a similar switch of the majority carrier with band edge reduction. It also matches recent developments in photodiodes operating at 1550 nm, where the *p*-type layer is made of materials with wider band gaps, a choice that appears rather driven by the necessity to maintain hole extraction than by optical design considerations. [33] With a band edge at 1550 nm and TBAI ligands, we even observed the Fermi level in the conduction band, indicative of degenerate doping. This finding is consistent with recent observations of intraband absorption in large iodine-treated PbS CQDs. [34,35]

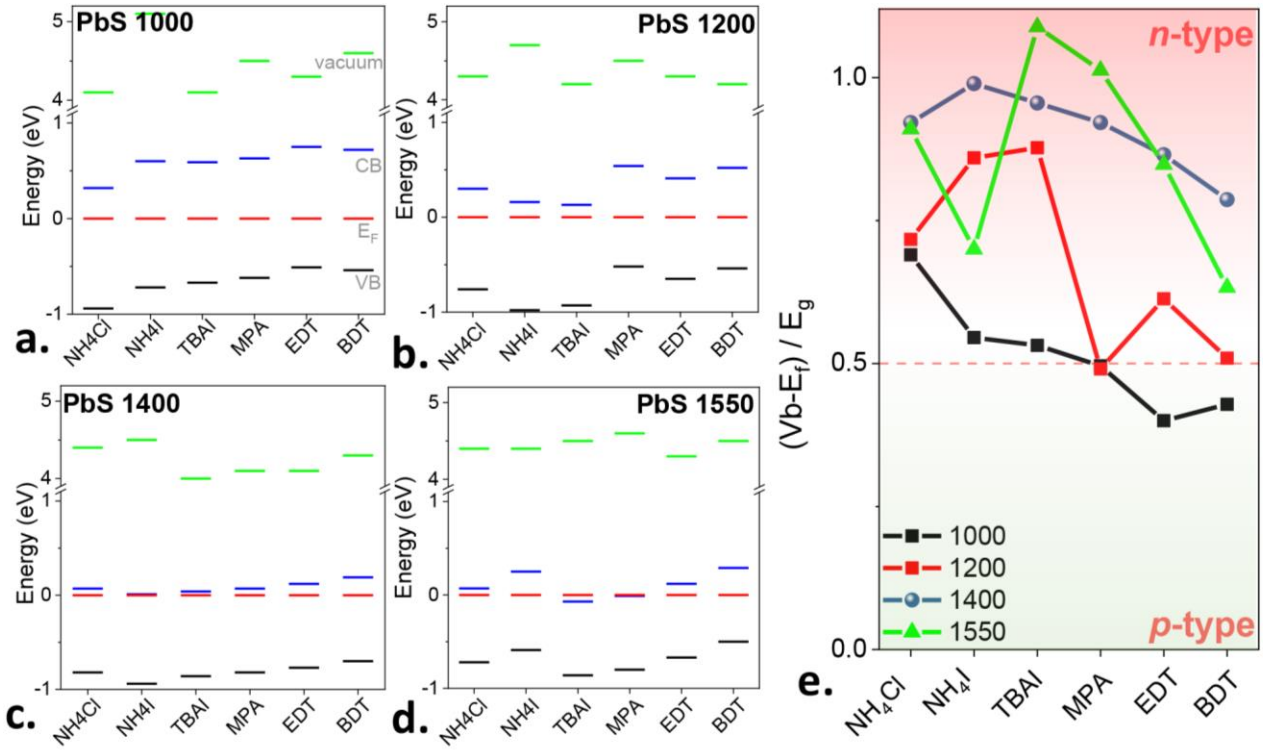

Figure 3 Reconstructed energy diagrams. *a. Energy diagram for PbS CQD with a band edge at 1000 nm and various capping ligands. Fermi energy (in red) is set at 0 eV. Valence band maximum is in black. Conduction band minimum (in blue) is determined by adding the optical gap to the valence band maximum. The vacuum level (in green) is determined from the work function value. b-d are the same sets of data for PbS 1200, 1400 and 1550 nm, respectively. Numeric values for this set of data are given in Table S2. e. Relative position of the Fermi level with respect to the band gap for all PbS CQD sizes. Fermi level in the bottom part of the graph corresponds to a p-type material, whereas Fermi level in the upper part of the graph is associated with an n-type character. Value above 1 corresponds to degenerate n-type doping.*

In this effective energy diagram, the displacement of the bands relative to the Fermi level is attributed to ligand-induced dipoles, moving the bands according to equation (1). However, there are aspects missed by UPS-type analysis that can be better understood by examining the core levels, as depicted in **Figure 4**a-d. The Pb 4f state typically exhibits three contributions. The main one (80-90% in weight) appears at around 138.3 eV and corresponds to lead coupled to sulfide. A second feature appears at a higher binding energy, indicating a less electron-rich lead environment attributed to lead chloride, due to chloride's higher electronegativity compared to sulfide. This contribution becomes significant when chloride is used as a ligand, as it is the case with NH_4Cl, and for smaller CQDs (**Figure 4**a) where leftover precursors are due to incomplete chemical reactions. In specific cases, such as with TBAI ligands, a third contribution emerges at 137.3 eV, attributed to metallic lead (Pb^0).[36] The presence of metal in the sample can be detrimental as it quenches excitons. This indicates that, in addition to the dipole effect, ligands can induce charge transfer, primarily at the surface, as evidenced by the relative weight of the Pb^0 peak decreasing with particle size. It's noteworthy that counterions seem to play a clear role in this charge transfer, as NH_4I-treated samples show no significant contribution from Pb^0.

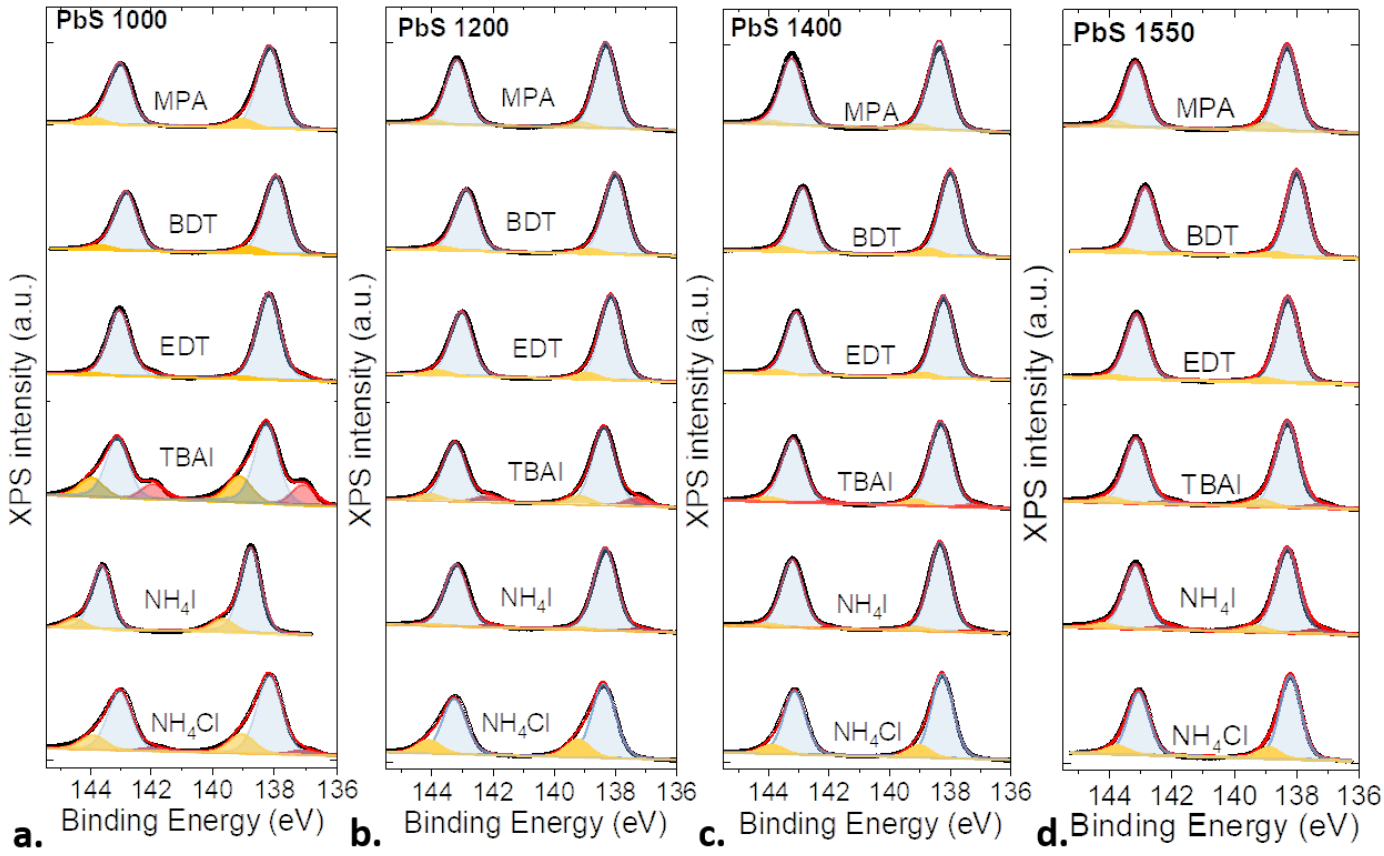

Figure 4 Pb 4f core level analysis *for various ligands capping PbS CQD with 1000 nm (a.), 1200 nm (b.), 1400 nm (c.) and 1550 nm (d.) band-edge, respectively. Fitting reveals the presence of three contributions. The main one (light blue) is associated with lead coupled to sulfide. The second contribution (yellow) appearing at higher binding energy is associated with lead coupled to chloride due to stronger electronegativity of chloride with respect to sulfide. Finally, the third one (red) appearing at lower binding energy is attributed to metallic lead (Pb^0). The red line corresponds to the sum of the three contributions.*

Due to the challenges associated with the use of ligands to build a *pn* junction in narrow band gap PbS CQDs, we explored the potential of remote doping. Previous proposals[37] for photodiodes and imagers at 1300 nm involved coupling a layer of PbS to electron (TiO_2[38]) and hole (NiO) transport layers. To quantify the potential of this approach, we directly measured the built-in potential using photoemission microscopy. A soft X-ray beam (95 eV) from the Soleil synchrotron (Antares beamline) was focused using a Fresnel zone plate, resulting in a 700 nm wide spot at the sample level. The sample was scanned in the x-y plane, and spectra were collected at each point, as shown in the schematic in **Figure 5**a. This setup posed two constraints: first, the lenses, designed to function with a monochromatic photon energy of around 100 eV, were not suitable for collecting the Pb 4f state, typically acquired at higher photon energies. Therefore, we focused on low energy states such as Pb 5d (Figure S28), which has a binding energy of around 18 eV. Secondly, the method, relying on soft X-rays, had a very limited photoelectron escape depth (few nm), which meant it could only probe the sample's surface. As a result, it was not well-suited for conventional vertical geometry diodes, which led us to focus on a planar version of the junction.[39] The fabrication procedure for the planar junction is outlined in Figure S27. Briefly, a Si/SiO_2 wafer was initially covered with a gold layer to minimize sample charging. The entire substrate was then coated with TiO_2. Subsequently, the substrate was spatially functionalized using conventional optical lithography technique, and a Ni layer was deposited. The Ni layer was oxidized, at least on the surface, to create a hole transport layer of NiO. Finally, a thin film of PbS CQDs was deposited on the substrate through a spin-coating

technique. An optical image of the device is shown in **Figure 5**b. Using photoemission microscopy, we tracked the Pb 5d state and mapped its energy shift over the structure, as depicted in **Figure 5**c. We are able to clearly correlate the distribution of the two transport layers with the potential of the coated semiconductor. On the TiO_2 layer, the Pb 5d state shifted toward a higher binding energy, as seen in **Figure 5**d, indicating a stronger n-type character.

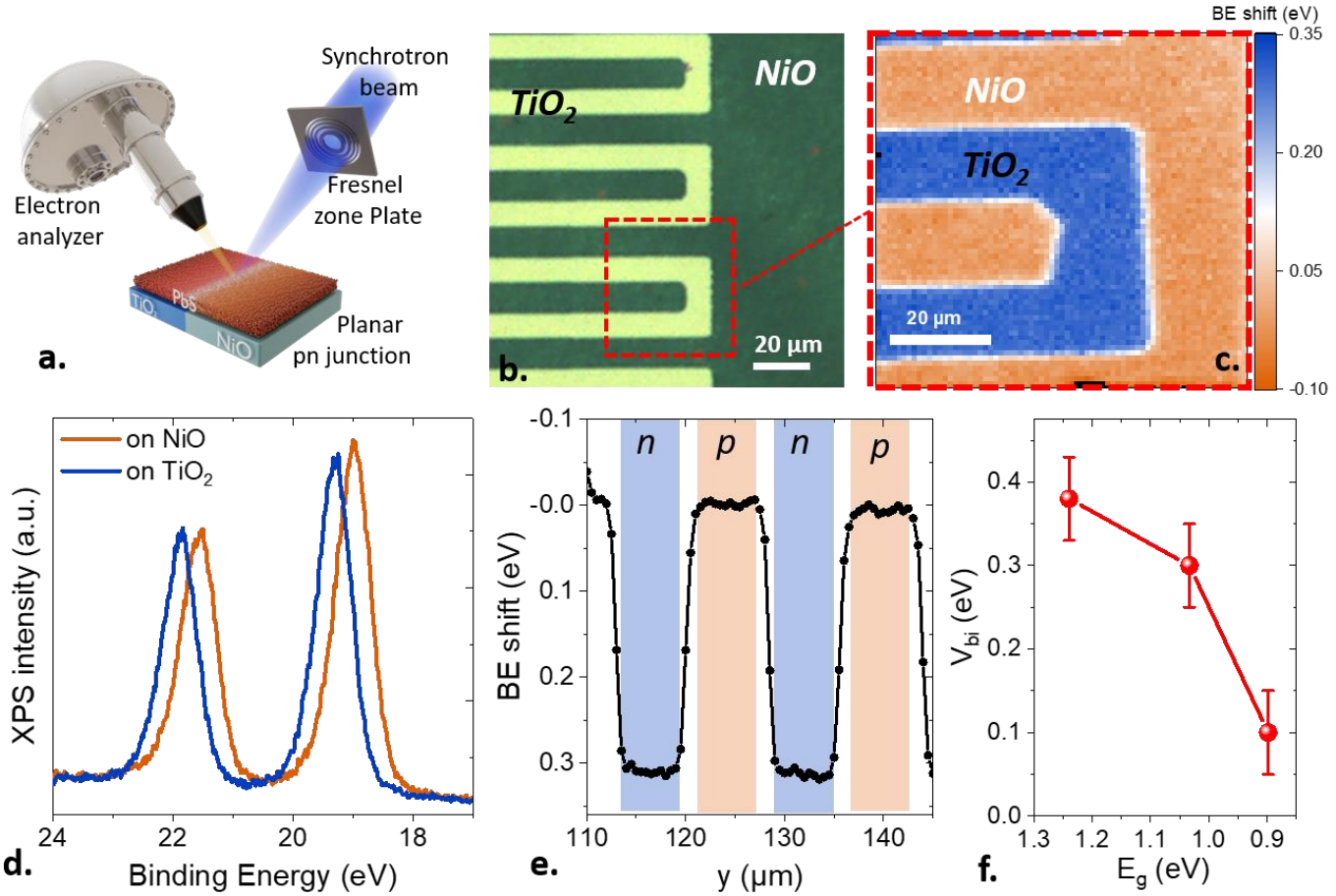

Figure 5 Photoemission microscopy used to reveal built-in potential*. a. Schematic of the experiment in which synchrotron beam (hv=95 eV) is focused using a Fresnel zone plate on the sample that is scanned. For each position a spectrum is acquired with the electron analyzer. b. Optical microscopy image of the planar interdigitated TiO_2/NiO junction. NiO appears darker on this image. c. Map of the energy shift of the Pb 4f state (the BE reference is taken on NiO, i.e. zero shift) over the area depicted in red dashed line in b. d. Pb 5d spectra over NiO and over TiO_2. e. Binding energy shift of the Pb 5d state as we scan perpendicular to the digit (i.e., y coordinate) of the structure. Data for c-e are reported for PbS 1200. f. Built-in potential over the junction as a function of the band gap energy.*

The transition from *n* to *p* domains occurs over 1-2 µm (**Figure 5**e), hence one can wonder if this domain corresponds to the space charge region. In a *pn* junction, the depletion width is given by $W=\left[\frac{2\varepsilon_0\varepsilon_r}{e}.\left(\frac{N_A+N_D}{N_AN_D}\right).(V_{bi}-V)\right]^{1/2}$ with *e* the elementary charge, N_A and N_D the acceptor and donor carrier density, V_{bi} the built-in potential and *V* the applied bias. From **Figure 3**, we learn that for the narrow band gap material, the material becomes strongly *n*-type, and thus $N_D \gg N_A$, which simplify previous equation for $W=\left[\frac{2\varepsilon_0\varepsilon_r}{N_Ae}.(V_{bi}-V)\right]^{1/2}$. Under zero bias (V=0 V) if we consider a W=1 µm, we found very low donor density (<10^{-15} cm^{-3}), which contradicts the earlier hypothesis that the material should be nearly degenerately doped. Thus, we can exclude the possibility that the extended

transition between the two domains is due to a depletion width and instead attribute it to the spatial resolution (around 1 µm) of the optical lithography used to define the NiO pattern.

We also examined the built-in potential for various band gap (PbS 1000, 1200 and 1400 nm), as depicted in **Figure 5**f. We observe a reduction in the energy shift with the band gap, ranging from nearly 400 meV to 100 meV. This reduction should be linked to the higher difficulty to generate p-type layer in large CQDs as evidenced from **Figure 3**. In this regard, this work demonstrates the need for narrow band gap PbS CQDs that are compatible with *p*-type doping. Alternatively, future effort should focus on heterojunction design. For example it has been noticed that for this band gap HgTe CQDs tend to be mostly *p*-type. [40]

Conclusion

We conducted a systematic investigation of the electronic structure of PbS CQDs whose band-edge is pertinent for emerging cost-effective infrared detection. Our study reveals that as the band gap narrows, the material shifts from having intrinsic behavior, which can be readily adjusted by surface chemistry, to exclusively exhibiting n-type nature. This transition continues until reaching a point where degenerate doping can occur, potentially leading to intraband absorption. Core level analysis further demonstrates that the role of ligands extends beyond dipole behavior; it can induce charge transfer effects, possibly leading to the formation of metallic islands detrimental to photodetection. Additionally, we employed photoemission microscopy to directly determine the built-in potential of a photodiode. Our findings show that the shift to an exclusively *n*-type nature for the largest PbS CQDs impacts the magnitude of the built-in potential. This necessitates novel strategies for designing short-wave infrared photodiodes relying on PbS CQDs

Supporting Information

Supporting Information include (*i*) analysis of valence band, cut-off of secondary electron, Pb 4f and S 2p core level for all samples, (*ii*) procedure to fabricate planar *pn* junction and (*iii*) discussion on photoemission microscopy measurements

COMPETING INTEREST

The authors declare no competing financial interests.

ACKNOWLEDEGMENTS

We thank Patrick Chervet (Onera) for performing simulation of the atmospheric transparency using software Matisse.[29] H.Z. thanks China scholar council for PhD funding. The project is supported by ERC grant blackQD (grant n° 756225) and AQDtive (grant n°101086358). We acknowledge the use of clean-room facilities from the “Centrale de Proximité Paris-Centre” and support from Renatech for micro and nanofabrication. This work was supported by French state funds managed by the ANR through the grants Frontal (ANR-19-CE09-0017), Graskop (ANR-19-CE09-0026), Copin (ANR-19-CE24-0022), Bright (ANR-21-CE24-0012-02), MixDferro (ANR-21-CE09-0029), Operatwist (ANR-22-CE09-0037-01) and E-map (ANR-23-CE50). This project has received financial support from the CNRS through the MITI interdisciplinary programs (project WITHIN).

REFERENCES

(1) Hines, M. A.; Scholes, G. D. Colloidal Pbs Nanocrystals with Size-Tunable Near-Infrared Emission: Observation of Post-Synthesis Self-Narrowing of the Particle Size Distribution. *Adv. Mater.* **2003**, *15*, 1844–1849.
(2) Weidman, M. C.; Beck, M. E.; Hoffman, R. S.; Prins, F.; Tisdale, W. A. Monodisperse, Air-Stable PbS Nanocrystals *via* Precursor Stoichiometry Control. *ACS Nano* **2014**, *8*, 6363–6371.
(3) Boles, M. A.; Engel, M.; Talapin, D. V. Self-Assembly of Colloidal Nanocrystals: From Intricate Structures to Functional Materials. *Chem. Rev.* **2016**, *116*, 11220–11289.
(4) Coropceanu, I.; Janke, E. M.; Portner, J.; Haubold, D.; Nguyen, T. D.; Das, A.; Tanner, C. P. N.; Utterback, J. K.; Teitelbaum, S. W.; Hudson, M. H.; et al. Self-Assembly of Nanocrystals into Strongly Electronically Coupled All-Inorganic Supercrystals. *Science* **2022**, *375*, 1422–1426.
(5) Weidman, M. C.; Nguyen, Q.; Smilgies, D.-M.; Tisdale, W. A. Impact of Size Dispersity, Ligand Coverage, and Ligand Length on the Structure of PbS Nanocrystal Superlattices. *Chem. Mater.* **2018**, *30*, 807–816.
(6) Winslow, S. W.; Tisdale, W. A.; Swan, J. W. Prediction of PbS Nanocrystal Superlattice Structure with Large-Scale Patchy Particle Simulations. *J. Phys. Chem. C* **2022**, *126*, 14264–14274.
(7) Xu, K.; Zhou, W.; Ning, Z. Integrated Structure and Device Engineering for High Performance and Scalable Quantum Dot Infrared Photodetectors. *Small* **2020**, *16*, 2003397.
(8) Lu, H.; Carroll, G. M.; Neale, N. R.; Beard, M. C. Infrared Quantum Dots: Progress, Challenges, and Opportunities. *ACS Nano* **2019**, *13*, 939–953.
(9) Dai, X.; Zhang, Z.; Jin, Y.; Niu, Y.; Cao, H.; Liang, X.; Chen, L.; Wang, J.; Peng, X. Solution-Processed, High-Performance Light-Emitting Diodes Based on Quantum Dots. *Nature* **2014**, *515*, 96–99.
(10) Nozik, A. J. Quantum Dot Solar Cells. *Phys. E Low-Dimens. Syst. Nanostructures* **2002**, *14*, 115–120.
(11) Moreels, I.; Lambert, K.; Smeets, D.; De Muynck, D.; Nollet, T.; Martins, J. C.; Vanhaecke, F.; Vantomme, A.; Delerue, C.; Allan, G.; et al. Size-Dependent Optical Properties of Colloidal PbS Quantum Dots. *ACS Nano* **2009**, *3*, 3023–3030.
(12) Aubert, T.; Golovatenko, A. A.; Samoli, M.; Lermusiaux, L.; Zinn, T.; Abécassis, B.; Rodina, A. V.; Hens, Z. General Expression for the Size-Dependent Optical Properties of Quantum Dots. *Nano Lett.* **2022**, *22*, 1778–1785.
(13) Brown, P. R.; Kim, D.; Lunt, R. R.; Zhao, N.; Bawendi, M. G.; Grossman, J. C.; Bulović, V. Energy Level Modification in Lead Sulfide Quantum Dot Thin Films through Ligand Exchange. *ACS Nano* **2014**, *8*, 5863–5872.
(14) Chehaibou, B.; Izquierdo, E.; Chu, A.; Abadie, C.; Cavallo, M.; Khalili, A.; Dang, T. H.; Gréboval, C.; Xu, X. Z.; Ithurria, S.; et al. The Complex Optical Index of Pbs Nanocrystal Thin Films and Their Use for Short Wave Infrared Sensor Design. *Nanoscale* **2022**, *14*, 2711–2721.
(15) Sklénard, B.; Mugny, G.; Chehaibou, B.; Delerue, C.; Arnaud, A.; Li, J. Size and Solvation Effects on Electronic and Optical Properties of PbS Quantum Dots. *J. Phys. Chem. Lett.* **2022**, *13*, 9044–9050.
(16) Chuang, C.-H. M.; Brown, P. R.; Bulović, V.; Bawendi, M. G. Improved Performance and Stability in Quantum Dot Solar Cells through Band Alignment Engineering. *Nat Mater* **2014**, *13*, 796–801.
(17) Kroupa, D. M.; Vörös, M.; Brawand, N. P.; McNichols, B. W.; Miller, E. M.; Gu, J.; Nozik, A. J.; Sellinger, A.; Galli, G.; Beard, M. C. Tuning Colloidal Quantum Dot Band Edge Positions Through Solution-Phase Surface Chemistry Modification. *Nat. Commun.* **2017**, *8*, 15257.
(18) Steckel, J. S.; Josse, E.; Pattantyus-Abraham, A. G.; Bidaud, M.; Mortini, B.; Bilgen, H.; Arnaud, O.; Allegret-Maret, S.; Saguin, F.; Mazet, L.; et al. 1.62µm Global Shutter Quantum Dot Image Sensor Optimized for Near and Shortwave Infrared. In *2021 IEEE International Electron Devices Meeting (IEDM)*; IEEE: San Francisco, CA, USA, 2021; p 23.4.1-23.4.4.

(19) Pejović, V.; Georgitzikis, E.; Lieberman, I.; Malinowski, P. E.; Heremans, P.; Cheyns, D. Photodetectors Based on Lead Sulfide Quantum Dot and Organic Absorbers for Multispectral Sensing in the Visible to Short-Wave Infrared Range. *Adv. Funct. Mater.* **2022**, *32*, 2201424.
(20) Pejovic, V.; Georgitzikis, E.; Lee, J.; Lieberman, I.; Cheyns, D.; Heremans, P.; Malinowski, P. E. Infrared Colloidal Quantum Dot Image Sensors. *IEEE Trans. Electron Devices* **2022**, *69*, 2840–2850.
(21) Lobo, A.; Möller, T.; Nagel, M.; Borchert, H.; Hickey, S. G.; Weller, H. Photoelectron Spectroscopic Investigations of Chemical Bonding in Organically Stabilized PbS Nanocrystals. *J. Phys. Chem. B* **2005**, *109*, 17422–17428.
(22) Garcia-Gutierrez, D. F.; Hernandez-Casillas, L. P.; Cappellari, M. V.; Fungo, F.; Martínez-Guerra, E.; García-Gutiérrez, D. I. Influence of the Capping Ligand on the Band Gap and Electronic Levels of PbS Nanoparticles through Surface Atomistic Arrangement Determination. *ACS Omega* **2018**, *3*, 393–405.
(23) Miller, E. M.; Kroupa, D. M.; Zhang, J.; Schulz, P.; Marshall, A. R.; Kahn, A.; Lany, S.; Luther, J. M.; Beard, M. C.; Perkins, C. L.; et al. Revisiting the Valence and Conduction Band Size Dependence of PbS Quantum Dot Thin Films. *ACS Nano* **2016**, *10*, 3302–3311.
(24) Clark, P. C. J.; Flavell, W. R. Surface and Interface Chemistry in Colloidal Quantum Dots for Solar Applications Studied by X-Ray Photoelectron Spectroscopy. *Chem. Rec.* **2019**, *19*, 1233–1243.
(25) Jasieniak, J.; Califano, M.; Watkins, S. E. Size-Dependent Valence and Conduction Band-Edge Energies of Semiconductor Nanocrystals. *ACS Nano* **2011**, *5*, 5888–5902.
(26) Bergeard, N.; Silly, M. G.; Krizmancic, D.; Chauvet, C.; Guzzo, M.; Ricaud, J. P.; Izquierdo, M.; Stebel, L.; Pittana, P.; Sergo, R.; et al. Time-resolved photoelectron spectroscopy using synchrotron radiation time structure. *J. Synchrotron Radiat.* **2011**, *18*, 245–250.
(27) Avila, J.; Razado-Colambo, I.; Lorcy, S.; Lagarde, B.; Giorgetta, J.-L.; Polack, F.; Asensio, M. C. ANTARES, a scanning photoemission microscopy beamline at SOLEIL. *J. Phys. Conf. Ser.* **2013**, *425*, 192023.
(28) Tang, J.; Kemp, K. W.; Hoogland, S.; Jeong, K. S.; Liu, H.; Levina, L.; Furukawa, M.; Wang, X.; Debnath, R.; Cha, D.; et al. Colloidal-Quantum-Dot Photovoltaics Using Atomic-Ligand Passivation. *Nat. Mater.* **2011**, *10*, 765–771.
(29) Labarre, L.; Croizé, L.; Fauqueux, S.; Huet, T.; Malherbe, C.; Pierro, J. MATISSE-V3.0: Overview and Future Developments; Carcassonne, 2016.
(30) Hendricks, M. P.; Campos, M. P.; Cleveland, G. T.; Jen-La Plante, I.; Owen, J. S. A Tunable Library of Substituted Thiourea Precursors to Metal Sulfide Nanocrystals. *Science* **2015**, *348*, 1226–1230.
(31) Moulder, J. F.; Stickle, W. F.; Sobol, P. E.; Bomben, K. D. *Handbook of X-Ray Photoelectron Spectroscopy*; Perkin-Elmer Corporation: USA, 1992.
(32) Choi, H.; Ko, J.-H.; Kim, Y.-H.; Jeong, S. Steric-Hindrance-Driven Shape Transition in PbS Quantum Dots: Understanding Size-Dependent Stability. *J. Am. Chem. Soc.* **2013**, *135*, 5278–5281.
(33) Vafaie, M.; Fan, J. Z.; Morteza Najarian, A.; Ouellette, O.; Sagar, L. K.; Bertens, K.; Sun, B.; García De Arquer, F. P.; Sargent, E. H. Colloidal Quantum Dot Photodetectors with 10-ns Response Time and 80% Quantum Efficiency at 1,550 nm. *Matter* **2021**, *4*, 1042–1053.
(34) Ramiro, I.; Kundu, B.; Dalmases, M.; Özdemir, O.; Pedrosa, M.; Konstantatos, G. Size- and Temperature-Dependent Intraband Optical Properties of Heavily n-Doped PbS Colloidal Quantum Dot Solid-State Films. *ACS Nano* **2020**, *14*, 7161–7169.
(35) Ramiro, I.; Özdemir, O.; Christodoulou, S.; Gupta, S.; Dalmases, M.; Torre, I.; Konstantatos, G. Mid- and Long-Wave Infrared Optoelectronics via Intraband Transitions in PbS Colloidal Quantum Dots. *Nano Lett.* **2020**, *20*, 1003–1008.
(36) Amelot, D.; Rastogi, P.; Martinez, B.; Gréboval, C.; Livache, C.; Bresciani, F. A.; Qu, J.; Chu, A.; Goyal, M.; Chee, S.-S.; et al. Revealing the Band Structure of FAPI Quantum Dot Film and Its Interfaces with Electron and Hole Transport Layer Using Time Resolved Photoemission. *J. Phys. Chem. C* **2020**, *124*, 3873–3880.

(37) Liu, J.; Liu, P.; Chen, D.; Shi, T.; Qu, X.; Chen, L.; Wu, T.; Ke, J.; Xiong, K.; Li, M.; et al. A Near-Infrared Colloidal Quantum Dot Imager with Monolithically Integrated Readout Circuitry. *Nat. Electron.* **2022**, *5*, 443–451.
(38) Gréboval, C.; Rastogi, P.; Qu, J.; Chu, A.; Ramade, J.; Khalili, A.; Dabard, C.; Dang, T. H.; Cruguel, H.; Ouerghi, A.; et al. Time-Resolved Photoemission to Unveil Electronic Coupling Between Absorbing and Transport Layers in a Quantum Dot-Based Solar Cell. *J. Phys. Chem. C* **2020**, *124*, 23400–23409.
(39) Cavallo, M.; Alchaar, R.; Bossavit, E.; Zhang, H.; Dang, T. H.; Khalili, A.; Prado, Y.; Silly, M. G.; Utterback, J. K.; Ithurria, S.; et al. Inside a Nanocrystal-Based Photodiode Using Photoemission Microscopy. *Nanoscale* **2023**, *15*, 9440–9448.
(40) Chu, A.; Martinez, B.; Ferré, S.; Noguier, V.; Gréboval, C.; Livache, C.; Qu, J.; Prado, Y.; Casaretto, N.; Goubet, N.; et al. HgTe Nanocrystals for SWIR Detection and Their Integration up to the Focal Plane Array. *ACS Appl. Mater. Interfaces* **2019**, *11*, 33116–33123.

TOC graphic

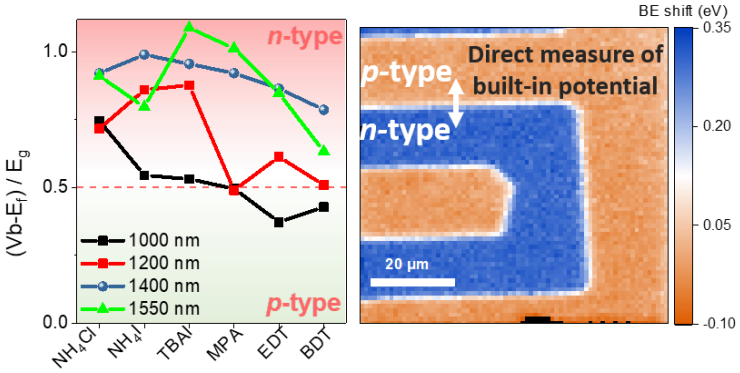
n-type
p-type
1000 nm
1200 nm
1400 nm
1550 nm
(Vb-Ef) / Eg
1.0
0.5
0.0
NH4Cl
NH4I
TBAI
MPA
EDT
BDT
BE shift (eV)
0.35
0.20
0.05
-0.10
p-type
n-type
Direct measure of
built-in potential
20 μm